The Young Planetary System K2-25: Constraints on Companions and Starspots

Isabel J. Kain[1,2] , Elisabeth R. Newton[2,3] , Jason A. Dittmann[2] , Jonathan M. Irwin[4], Andrew W. Mann[5] , Pa Chia Thao[5] ,
David Charbonneau[4] , and Jennifer G. Winters[4]

[1] Department of Physics, Northeastern University, Boston, MA 02115, USA; kain.i@husky.neu.edu, ijkain@gmail.com
[2] Kavli Institute for Astrophysics and Space Research, Massachusetts Institute of Technology, Cambridge, MA 02139, USA
[3] Department of Physics and Astronomy, Dartmouth College, Hanover, NH 03755, USA
[4] Harvard-Smithsonian Center for Astrophysics, Cambridge, MA 02138, USA
[5] Department of Physics and Astronomy, University of North Carolina at Chapel Hill, Chapel Hill, NC 27599, USA

Abstract

The abundance of planets with orbital periods of a few to tens of days suggests that exoplanets experience complex dynamical histories. Planets in young stellar clusters or associations have well-constrained ages and therefore provide an opportunity to explore the dynamical evolution of exoplanets. K2-25b is a Neptune-sized planet in an eccentric, 3.48 day orbit around an M4.5 dwarf star in the Hyades cluster (650 Myr). In order to investigate its non-zero eccentricity and tight orbit, we analyze transit timing variations (TTVs) which could reveal clues to the migration processes that may have acted on the planet. We obtain 12 nonconsecutive transits using the MEarth observatories and long-term photometric monitoring, which we combine with 10 transits from the *Spitzer* Space Telescope and 20 transits from *K2*. Tables of MEarth photometry accompany this work. We fit each transit lightcurve independently. We first investigate whether inhomogeneities on the stellar surface (such as spots or plages) are differentially affecting our transit observations. The measured transit depth does not vary significantly between transits, though we see some deviations from the fiducial transit model. We then looked for TTVs as evidence of a nontransiting perturber in the system. We find no evidence for $>1\,M_\oplus$ mass companions within a 2:1 period ratio, or for $>5\,M_\oplus$ mass planets within a 7:2 period ratio.

Unified Astronomy Thesaurus concepts: Exoplanet astronomy (486); Exoplanet systems (484); Exoplanet dynamics (490); Exoplanets (498); Hot Neptunes (754)

Supporting material: data behind figures

1. Introduction

Planetary migration is thought to play an important role in shaping the final architectures of planetary systems. For example, migration results in the highly visible population of hot Jupiters (Dawson & Johnson 2018) and also may explain the systems of tightly packed sub-Neptunes (Ford 2014).

The population of short-period planets includes a subset similar in radius to Neptune, sometimes referred to as hot Neptunes. There has been some speculation that hot Neptunes are part of a broader planet population that also includes hot Jupiters: perhaps the smaller close-in Neptunes are hot Jupiters that have been stripped of their atmospheres, or perhaps these two classes of planets share migration histories. Although mass-loss rates of 10^{11}–10^{12} g s^{-1} have been detected in hot Jupiters, the breakdown of energy-limited escape at high-incident fluxes suggests that Neptune-sized planets are not the remnants of close-in Jupiters (Murray-Clay et al. 2009). Dong et al. (2018) suggest common formation or migration histories, finding that hot Neptunes and hot Jupiters share a similar preference for singly transiting systems and metal-rich host stars.

Young exoplanets, which may be in the midst of their most dynamically active years, can provide unique insight into the origins of the planetary systems observed around typical field-aged stars (ages $\gtrsim 1$ Gyr). Our focus in this paper is the young exoplanet K2-25b (Mann et al. 2016), an eccentric ($e = 0.27$) short-period ($P = 3.48$ days) hot Neptune in a close orbit ($a = 0.035$ au) around a mid-M dwarf ($M_* = 0.26 M_\odot$, $R_* = 0.29 R_\odot$). K2-25 is a member of the Hyades cluster, the age of which is estimated to be approximately 650 Myr (Perryman et al. 1998; DeGennaro et al. 2009; Gossage et al. 2018; Martín et al. 2018). We note that Brandt & Huang (2015) and

Gaia Collaboration et al. (2018) have suggested an 800 Myr age for the Hyades (see Gossage et al. 2018, for further discussion).

Mann et al. (2016) and David et al. (2016) independently identified K2-25b using data from the K2 ecliptic plane survey. Though the sampling of *K*2 data is such that this short transit is poorly resolved in the 30 minute cadence *K*2 data, Mann et al. (2016) were able to validate the planet using high-contrast imaging, radial velocity measurements, and statistical arguments. The short duration of the transit and constraints on the stellar density suggested that K2-25b is on an eccentric orbit, an effect which is sometimes called the photoeccentric effect (e.g., Barnes 2007; Ford et al. 2008; Dawson & Johnson 2012). In a companion paper, Thao et al. (2020) update the stellar parameters using the new *Gaia* parallax, and report a moderate eccentricity for K2-25b via this effect by simultaneously modeling all observed transits (Table 1). Given the star's youth and the clear 1.88 day photometric rotational modulation seen in the *K*2 discovery lightcurve, we note the possibility of starspots impacting the transit parameters.

K2-25b may represent a precursor of the hot Neptunes found around older stars. A notable example is Gl 436b (Butler et al. 2004), which is also a short-period Neptune-sized planet with a non-zero eccentricity. The origin of Gl 436b's high eccentricity remains unclear, though both Kozai migration spurred by a distant companion (Bourrier et al. 2018) and continuous excitation by a planetary companion that is not in a near mean-motion resonance (Batygin et al. 2009) have been explored as possible explanations for these characteristics. However, no exterior companion has been detected to date. In

Table 1
Parameters for K2-25b Used in Analysis

Parameter	Value
Period (days)	3.4845638
T_0 (BJD)	2457062.57958
r_P/R_*	0.10807
ρ_*	10.597
$\sqrt{e}\sin w$	0.405
$\sqrt{e}\cos w$	0.219
b	0.655
$q_{1,\mathrm{MEarth}}$	0.288
$q_{2,\mathrm{MEarth}}$	0.188
$q_{1,\mathrm{SpitzerCH1}}$	0.124
$q_{2,\mathrm{SpitzerCH1}}$	0.161
$q_{1,\mathrm{SpitzerCH2}}$	0.113
$q_{2,\mathrm{SpitzerCH2}}$	0.159
$q_{1,\mathrm{K2}}$	0.559
$q_{2,\mathrm{K2}}$	0.270

Note. Planetary parameters for K2-25b adopted in this work, which are the maximum of the posterior distributions from the combined fit from Thao et al. (2020). q are the limb-darkening parameterization from Kipping (2013).

contrast, the close-orbiting Neptune mass planet HD 219828b (Melo et al. 2007) has an eccentricity consistent with zero, but the system includes an outer, highly eccentric planet or brown dwarf that likely influenced its dynamical evolution (Santos et al. 2016).

We present new transit observations and long-term photometric monitoring of K2-25b obtained using the MEarth observatories in order to probe the impact of starspots on our transit data and to look for nontransiting companions via transit timing variations (TTVs; Holman & Murray 2005; Agol et al. 2004). We combine our data with transits observed from the *Spitzer* and *K2* space telescopes (Section 2). We detail our analysis method, in which we fit each transit independently (Section 3). We test for the impact of stellar surface inhomogeneities on the measured transit properties (Section 4) and look for evidence of companions using TTVs (Section 5). We conclude by discussing K2-25b in the context of planet migration scenarios (Section 6) and presenting a brief summary of our work (Section 7).

Throughout this work, we will denote individual transits by the transit number, counting up from the transit ephemeris given in Mann et al. (2016).

2. Data

2.1. Space-based Photometry from Spitzer and K2

K2-25 was observed by the *Kepler* spacecraft in Campaign 4, between 2015 February 8 and 2015 April 20 at a 30 minute cadence. We downloaded the lightcurves available on the Mikulski Archive for Space Telescopes on 7 September 2018. After examining the different data reductions available we use data from the K2SC algorithm (Aigrain et al. 2016). We manually inspected each transit within a 4 hr window to either side of the transit mid-point and discarded six transits for which there were clear signs of a flare; this inspection was completed without regard to the quality of the transit fit.

Thao et al. (2020) obtained transit observations with *Spitzer*; these data and the corresponding analyses will be presented in detail in that work. To briefly summarize, *Spitzer* observed 10 full transits of K2-25b, five in each of 3.6 μm and

Table 2
Mid-transit Times

Transit Number	Mid-transit Time (BJD)	Telescope
0	$2457062.581263^{+0.000348}_{-0.000337}$	*K2*
1	$2457066.065295^{+0.000342}_{-0.000300}$	*K2*
2	$2457069.547610^{+0.000373}_{-0.000366}$	*K2*
3	$2457073.034524^{+0.000392}_{-0.000385}$	*K2*
4	$2457076.517230^{+0.000328}_{-0.000329}$	*K2*
5	$2457080.003011^{+0.000368}_{-0.000346}$	*K2*
6	$2457083.486753^{+0.000389}_{-0.000364}$	*K2*
10	$2457097.424917^{+0.000371}_{-0.000373}$	*K2*
12	$2457104.394692^{+0.000387}_{-0.000372}$	*K2*
14	$2457111.364489^{+0.000385}_{-0.000388}$	*K2*
15	$2457114.847241^{+0.000447}_{-0.000386}$	*K2*
16	$2457118.333371^{+0.000348}_{-0.000346}$	*K2*
17	$2457121.818849^{+0.000557}_{-0.000598}$	*K2*
18	$2457125.300855^{+0.000290}_{-0.00293}$	*K2*
20	$2457132.270650^{+0.000475}_{-0.000417}$	*K2*
87	$2457365.736862^{+0.000172}_{-0.000170}$	MEarth
89	$2457372.705796^{+0.000273}_{-0.000255}$	MEarth
174	$2457668.893487^{+0.000344}_{-0.000345}$	MEarth
176	$2457675.862698^{+0.000204}_{-0.000202}$	MEarth
178	$2457682.831729^{+0.000230}_{-0.000233}$	MEarth
180	$2457689.801044^{+0.000227}_{-0.000231}$	MEarth
182	$2457696.769930^{+0.000260}_{-0.000265}$	MEarth
184	$2457703.738953^{+0.000186}_{-0.000188}$	MEarth
186	$2457710.708559^{+0.000195}_{-0.000194}$	MEarth
188	$2457717.677520^{+0.000172}_{-0.000169}$	MEarth
189	$2457721.162269^{+0.000155}_{-0.000152}$	Spitzer
190	$2457724.646792^{+0.000202}_{-0.000202}$	MEarth
191	$2457728.131147^{+0.000164}_{-0.000161}$	Spitzer
192	$2457731.615021^{+0.000158}_{-0.000153}$	Spitzer
192	$2457731.616424^{+0.000679}_{-0.000628}$	MEarth
193	$2457735.100594^{+0.000173}_{-0.000178}$	Spitzer
195	$2457742.069854^{+0.000210}_{-0.000210}$	Spitzer
196	$2457745.553921^{+0.000168}_{-0.000176}$	Spitzer
197	$2457749.038225^{+0.000174}_{-0.000170}$	Spitzer
198	$2457752.523305^{+0.000185}_{-0.000186}$	Spitzer
199	$2457756.007769^{+0.000142}_{-0.000142}$	Spitzer
236	$2457884.936644^{+0.000181}_{-0.000182}$	Spitzer

4.5 μm, both taken with the Infrared Array Camera (IRAC; Fazio et al. 2004) over the period of 2016 November 28 to 2017 May 11 (Program ID: 13037, PI: Mann). We extracted the lightcurves from the *Spitzer* data using using a high-resolution pixel variation gain map (PMAP; Ingalls et al. 2012) to correct for intrapixel sensitivity variations. Fits using other techniques for high-precision photometry with *Spitzer*, including nearest neighbors (Lewis et al. 2013) and pixel-level decorrelation (Deming et al. 2015) yielded similar results, although PMAP provided the lowest red noise and most consistent transit depths at a given wavelength across the transits.

2.2. Ground-based Photometry from the MEarth Observatories

We obtained lightcurves of K2-25 with the MEarth Observatories (Irwin et al. 2015). MEarth–North comprises eight 40 cm telescopes at the Fred Lawrence Whipple Observatory on Mount Hopkins, Arizona, and MEarth–South

is a near-twin located at the Cerro Tololo Inter-American Observatory in Chile. The MEarth CCDs are 2048 × 2048 pixels with pixels scales of 0″78 pixel^{-1} in the north and 0″84 pixel^{-1} in the south. All data presented here were observed using the Schott RG715 filter, the filter profile for which is available in Dittmann et al. (2016). Integration times of 60 s were used throughout, and the recorded observation time is the midpoint of the exposure. Photometric monitoring began on 2015 December 9, and this work includes data obtained through 2018 August 4. We monitored the brightness of the star using a single telescope from MEarth–South, obtained a set of back-to-back exposures twice nightly, with a typical time separation of 20 minutes. We observed 12 transits using between three and eight telescopes at both the northern and southern MEarth sites, during which the star was monitored continuously with a cadence of approximately 1.5 minutes. Three additional transits were observed, but are not analyzed due to the photometric precision and systematics; this data quality cut was performed prior to performing any transit depth or transit time analyses.

The MEarth data are reduced with standard differential aperture photometry using a pipeline based on Irwin et al. (2007) with differences described in the data release notes.[6] The data are analyzed as described in Newton et al. (2016); in brief, we simultaneously fit for variability induced by changes in precipitable water vapor, constant magnitude offsets, and the intrinsic stellar variability. The magnitude offsets result from reference stars being located on different parts of the detector when on either side of the meridian, a consequence of German Equatorial Mounts, and are also introduced to model otherwise unaccounted for changes in the flat field. The stellar variability is assumed to be a sinusoid of variable amplitude and phase. We perform the simultaneously fit across a grid of rotation periods and select the best-fitting period.

For MEarth transit observations, we independently reduce data obtained by a single telescope for a given transit. We first mask the transit, and fit the out-of-transit data to our rotation and systematics model. We fix the rotation period to the best-fitting value from our rotation analysis of data obtained from our long-term photometric monitoring, and fit only for the amplitude of the sinusoid and the scale factors that determine the contributions of the systematics. For most transits, the out-of-transit baseline is >2 hr both before and after the transit. We remove systematics but preserve the stellar variability. Data from all telescopes that observed a given transit are combined into a single lightcurve, preserving each datum without averaging.

2.3. Data not Analyzed

Thao et al. (2020) analyze two transits obtained from the Las Cumbres Observatory (LCO) as part of their joint fit. We do not use the LCO data in the present work because the precision on the individual transits is insufficient for transit timing analyses. We also do not analyze data from *K2*: due to the 30 minute sampling, neither transits nor stellar flares are fully resolved, which we found rendered modeling individual transit events challenging.

---

3. Transit Analysis

We fit each transit independently using batman (Kreidberg 2015), which implements the Mandel & Agol (2002) transit model, and emcee (Foreman-Mackey et al. 2013), an implementation of the affine-invariant Markov Chain Monte Carlo (MCMC) ensemble sampler proposed by Goodman & Weare (2010). For the MEarth data, we use data within 2.5 hr of the transit midpoint or the maximum available baseline, whichever is greater. We remove 3σ outliers. Stellar variability has not be removed in either data set. Our fits for the *Spitzer* and MEarth transits are shown in Figure 1.

We use batman to generate our lightcurve model. The model consists of the transit midpoint (T); the planet's period (P), radius ratio (r_P/R_*), semimajor axis ratio (a/R^*), inclination (i), eccentricity (e), and argument of periastron (ω); and the star's limb-darkening coefficients ($q1$ and $q2$). We additionally include a constant offset (A) and a linear term (B) to account for trends in the flux levels presumed to be related to stellar rotation (the maximum observing window spans one-tenth of the stellar rotation period). All fixed parameters are set to the maximum posterior values of the combined fit of Thao et al. (2020), listed in Table 1.

We perform two fits to our data. (1) We fix all parameters except for the planetary parameters T and r_P/R_*, and the variables A and B. These fits are used in Section 4 to assess the potential for spots impacting our transit measurements. (2) We fix all parameters except for T, A, and B. These fits are used in Section 5 for our transit timing analysis. We use a uniform prior on all parameters. We use an ensemble of 30 walkers and first run 100,000 steps with an 80,000-step burn-in, which are discarded. The remaining 20,000 steps are used to create our final probability distributions.

4. Starspots on K2-25

Stellar surface inhomogeneities, such as spots, faculae, and plages, result in variations on timescales related to the stellar rotation period, and can affect the transit lightcurve. For example, if the path of transit crosses a bright region, it will cause an extra drop in brightness. Individual crossings can sometimes be clearly discerned in a lightcurve (Dittmann et al. 2009; Sanchis-Ojeda & Winn 2011). However, if crossings of dark (or bright) regions are not identified and attributed to the transiting planet, one will conclude that the planet has a smaller (or larger) radius than it actually does. In the models in Rackham et al. (2018, their Table 5), a hot Neptune transiting an M4V star with solar-like spots and faculae (the scenario producing the largest stellar signal) appears to have r_P/R_* larger than the unspotted case by $r_P/R_* = 0.005$.

4.1. Long-term Variability

Figure 2 shows the long-term variability of K2-25, with phase-folded lightcurves from MEarth. The star has a rotation period of 1.88 days and a peak-to-peak photometric amplitude of close to 2% in the MEarth lightcurve (it is similar in *K2*). This is typical for rapidly rotating mid-M dwarfs (Douglas et al. 2014; Newton et al. 2016). The photometric amplitude remained high throughout the 90 day *K2* campaign and the first year (2015–2016) of the ground-based monitoring from MEarth, and maintained a consistent morphology.

The variability models from Rackham et al. (2018) suggest that the 2% variability could be explained by either a $\gtrsim$30% covering
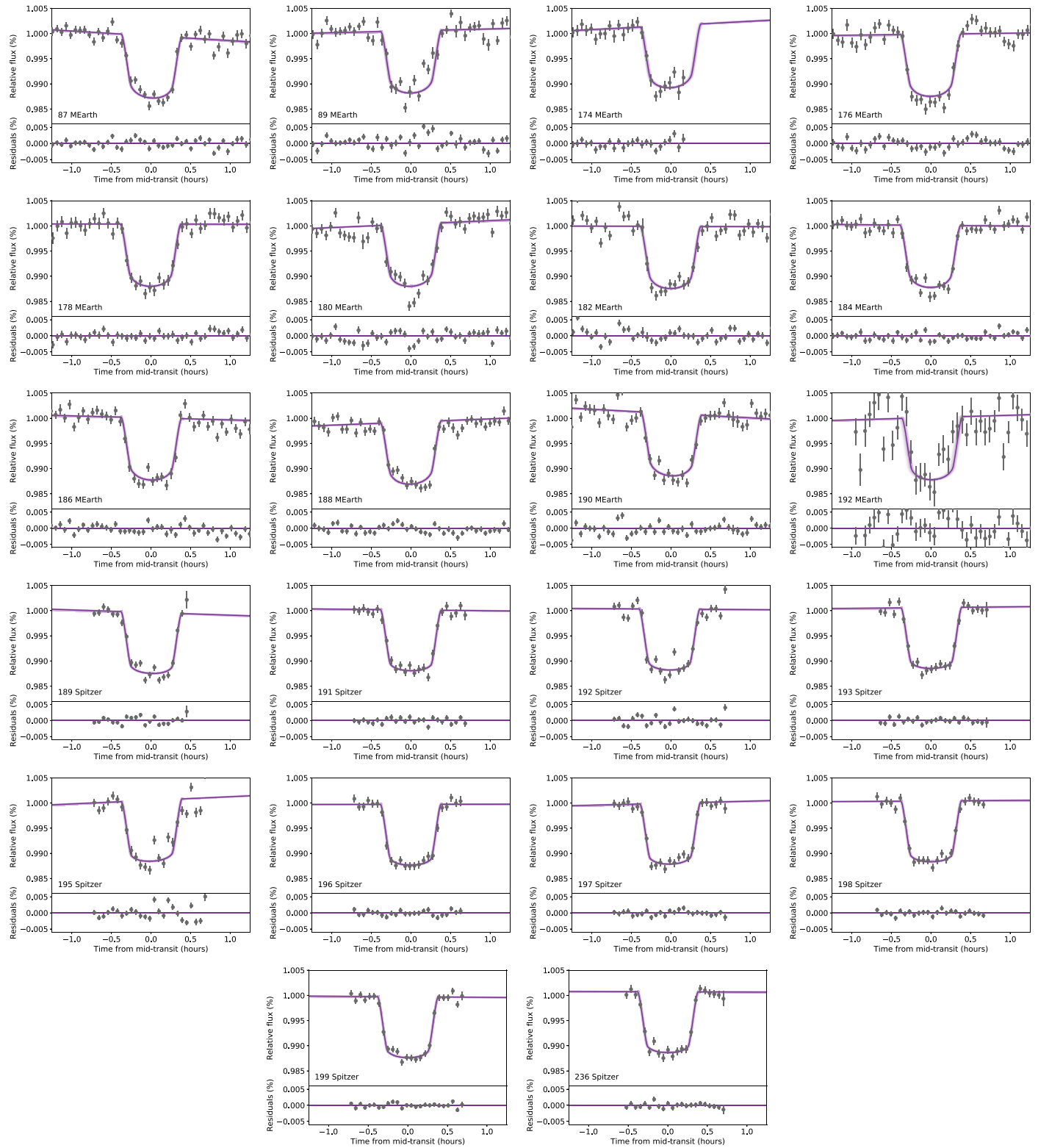
Figure 1. Best fit and residuals for *Spitzer* and MEarth transits from our MCMC analysis, fitting only for *T* (Section 3). The data are uncorrected for stellar variability. The horizontal axis is the time from the transit mid-point in hours and the vertical axis is the relative flux. Each lightcurve is centered at the mid-transit time expected from a linear ephemeris and the planet period from Mann et al. (2016). The data has been binned to 3.5 minutes. The panels are denoted by the number of transits since the ephemeris and the observatory. Note that transit 192 was observed twice, with both *Spitzer* and MEarth.

(The data used to create this figure are available.)

fraction of small spots, or a ≲10% covering fraction of large spots. In 2016–2017, the phase shifts and the amplitude decreases by half, and in 2017–2018 the amplitude increases slightly and acquires a double dip. This could result from fewer spots, but as noted in Basri (2018), the decrease in photometric variability could instead correspond to a rearrangement in spots.
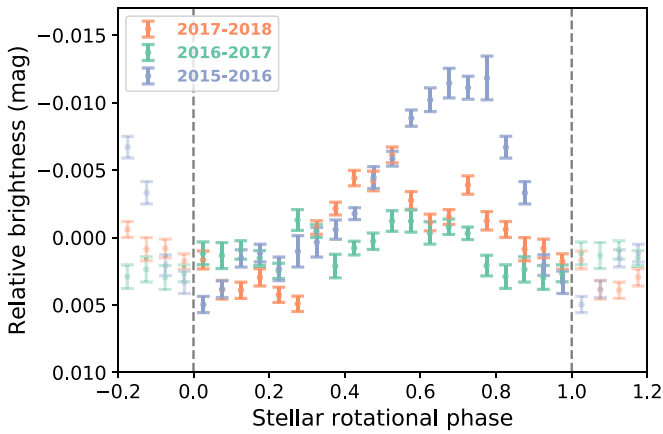
Figure 2. Stellar rotational variability over three years, folded on the stellar rotation period and averaged in 20 evenly spaced bins in phase. The data are separated into three time periods that correspond to observing seasons; phase-folded data from each season are averaged separately and plotted in different colors. While our photometric monitoring for rotation spans three observing seasons from 2015 to 2018, the majority of our transit observations (Figure 3) were collected in the 2016–2017 observing season, which corresponds to a time of lower stellar photometric variability.

(The data used to create this figure are available.)

Figure 3. Inferred planet radius as a function of stellar rotation phase. Each point corresponds to a different transit observation. The color of the points indicates the observing season in which the transit took place and match the colors in Figure 2; the majority of transits were observed in 2016–2017, which was a time of low photometric variability. Circles indicate transits obtained using MEarth, and squares are transits obtained using *Spitzer*. Significant interference in the transit lightcurve due to spot configuration could be indicated by outliers in this diagram or by a correlation between phase and r_P/R_*. Four outliers are marked in the figure and discussed further in Section 4. No correlation is apparent.

4.2. Transit Depth Variations and Spot Crossings

In Figure 3, we consider the inferred planet radius r_P/R_* as a function of stellar rotational phase. The results in this figure are derived from our fit varying both r_P/R_* and T. Most transit data from MEarth and all data from *Spitzer* were obtained when K2-25 was in a low-variability phase. The data show consistent transit depths across most transits: if our transit depths are impacted by stellar surface inhomogeneities, there is not a strong time-dependent component. Four outliers are denoted by the transit number in Figure 3 and discussed further in this section. We also generally found in-transit deviations to be similar to the out-of-transit variations in all transits except for MEarth 87, which we comment on below.

For two outliers, we suggest that the transit depth differences are due to unaccounted for errors. MEarth 176, for which the transit is deep, has strong systematic variability visible in the post-transit data, which could be impacting the depth measurement. MEarth 192, for which the transit is shallow, is our noisiest lightcurve and a simultaneous *Spitzer* transit has a normal transit depth.

For the other two outliers, spots may be responsible for the transit depth differences. These transits are shown in Figure 4, and compared to maximum posterior fit from the combined transit model from Thao et al. (2020). MEarth 89 corresponds to one of only two transits observed 2015–2016, during K2-25's high-variability phase. The transit is noticeably shallower than the model from Thao et al. (2020). This could indicate that the transit chord at this moment is darker than the unocculted stellar surface. However, we note that the post-transit data is impacted by scatter beyond the photometric errors. Also shown in Figure 4 is the other transit obtained in 2015–2016 (MEarth 87), which has a transit depth consistent with the others, but shows an asymmetry during ingress. Finally, in *Spitzer* 195, we see a candidate crossing of a dark spot. However, during this transit, the target did not fall on the sweet spot of the *Spitzer* detector, and uncharacterized systematics are of concern.
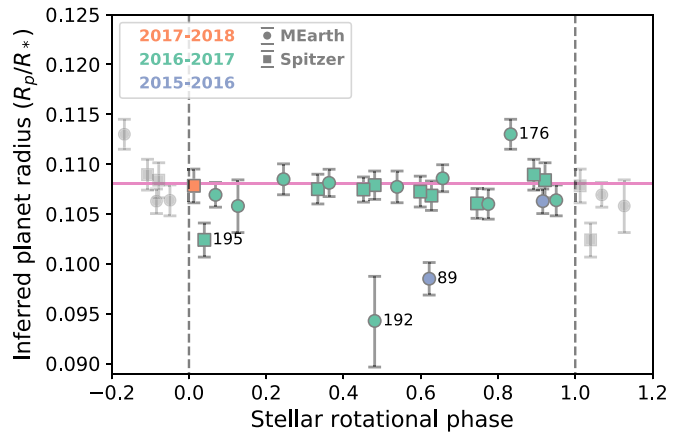
While the measured transit depths are not significantly different, we also noted candidate spot crossings in MEarth 180. However, systematics are again of concern.

5. Constraints on Companions

An unperturbed planet orbiting its star will take the same amount of time to complete each revolution around its star, with small exceptions for orbital precession or tidal decay. However, when a companion is added to the system, mutual gravitational interaction causes the two (or more) planets to exchange energy and angular momentum. This causes short-term oscillations of the semimajor axes and eccentricities of these planets, which in turn leads to variations in the time interval between transits. For example, the first positive detections of TTVs in an exoplanetary system was observed for *Kepler*-19b (Ballard et al. 2011), which consists of a $2.2\,R_\oplus$ planet on a 9.3 day orbit around a Sun-like star. The transit times of *Kepler*-19b showed sinusoidal-like variations indicating the presence of at least one nontransiting companion at a longer period.

5.1. Planet Mass Estimation

An approximate planet mass is necessary for TTV analysis. We use the nonparametric mass–radius relationship from Ning et al. (2018) implemented in the publicly available package MRExo[7] (Kanodia et al. 2019). We use the provided results from the *Kepler* data set to predict the planet's mass given its radius; this data set includes exoplanets with mass from both radial velocities and N-body dynamical fits to TTV. Using the planetary radius and error from Thao et al. (2020), we estimate a mass of $7^{+10}_{-4}\,M_\oplus$ for K2-25b, where the error bars represent the 68% confidence interval. The mass–radius relation for sub-Neptunes from Wolfgang et al. (2016), $M/M_\oplus = 2.7(R/R_\oplus)^{1.3}$, yields $M_P = 13.5 \pm 1.9\,M_\oplus$ where the error is dominated by the intrinsic scatter in the relationship.

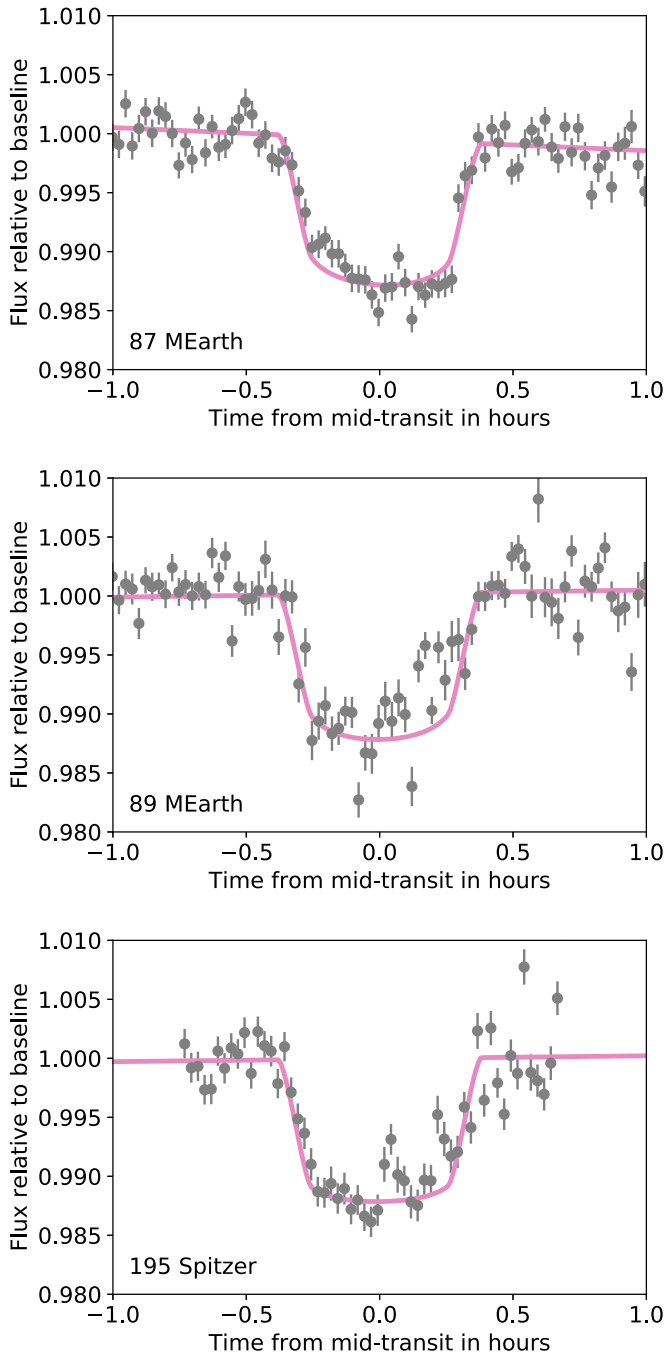---

[7] https://github.com/shbhuk/mrexo

Figure 4. Transit lightcurves of the three transits that show deviations from the transit model. MEarth 87 is shown on the top, MEarth 89 in the middle, and *Spitzer* 195 on the bottom. The data are binned using a robust weighted mean to 1.5 minutes. The model shown is the maximum posterior of the combined fit model from Thao et al. (2020), adjusted by our fits for *A* and *B* to account for overall changes in slope.

We note that when looking at planets in the sample from Ning et al. (2018) between 4 and 5 $R_{\oplus}$, there are a few outliers to the distribution at higher masses; while we adopt the mass from the Ning et al. (2018) mass–radius relation, we also comment on our expectations if K2-25b were to have a mass of 30 $M_{\oplus}$.

5.2. Transit Timing Analysis

We investigated whether the transit times of K2-25b, which we display in Figure 5 for the *Spitzer* and MEarth data, and

include in Table 2 for *Spitzer*, MEarth, and *K2* data, are consistent with an unperturbed linear ephemeris or whether there is evidence for additional near-resonant companions in this system. We follow a procedure similar to Dittmann et al. (2017).

Our observations comprise 39 individual transit observations over 822 days (236 orbits of K2-25b). The combination of ground-based MEarth transit measurements and space-based *Spitzer* measurements allow us to measure transit times of closely spaced transits at high precision. This dense sampling, combined with a long baseline from *K2* to establish the average period of K2-25b, allows us to fully sample the transit timing signal and assess whether there is evidence for another perturbing body.

The largest variation from a linear ephemeris present in our data is approximately 2 minutes in magnitude, and we see no evidence for a significant variation from a linear ephemeris. In order to determine what mass bodies we may exclude via transit timing, we use the `TTVFaster` code (Deck & Agol 2016), an extension of `TTVFast` (Deck et al. 2014) capable of estimating a TTV signal with eccentric planets.

We limit our TTV sensitivity analysis to be between periods of 0.5 days and 25 days (just beyond seven times the period of K2-25b). For each trial period, we initialize 500 versions of K2-25b drawn from the best-fit parameters determined by Thao et al. (2020) we have presented here. For each of these 500 systems, we initialize 500 versions of a possible K2-25 c. Each companion is drawn to have an eccentricity between 0 and 0.5 with uniform probability, an inclination angle relative to the star between 80 and 110 degrees with uniform probability, and random longitudinal nodes, argument of periastron, and mean anomalies. Initially, all perturbing planet masses are 0.5 $M_{\oplus}$.

For each system generated at each period, we sample the transit times of K2-25b at the timestamps of the observed data. We then fit a linear ephemeris to the generated transit times. This effectively marginalizes over planetary orbital parameters. If the 90th percentile of the amplitude of these TTVs is greater than the 2 minute deviation we observe in our data, then we adopt this mass value as our limiting value. Otherwise, we increase the mass of the perturber by 0.5 $M_{\oplus}$ and repeat the procedure until a sufficiently large TTV is observed.

We plot these maximum allowed perturbing mass as a function of the period ratio between a potential perturber and K2-25b in Figure 6. We find that the lack of TTVs in K2-25b precludes all but the shortest period companions interior to K2-25b. Furthermore, we can largely eliminate low-mass companions out to the 2:1 orbital resonance with K2-25b. Beyond orbital period ratios of 7:2 we require much higher mass perturbers to create a detectable TTV signal, and are largely insensitive to possible small bodies outside of strong integer resonances. We performed the same calculation using transit times measured from fits to individual *K2* transits and arrived at consistent results: the *K2* transit times are not precise enough to strongly impact our sensitivity to TTVs.

6. Discussion

The hot Neptune K2-25b arrived at and appears to have thus far maintained a close-in, moderately eccentric orbit. Eccentric systems may quickly circularize due to tidal forces. If the circularization timescale for this planet is close to or larger than the age of the system, then we are likely observing this planet in the act of circularizing after some single dynamic event early
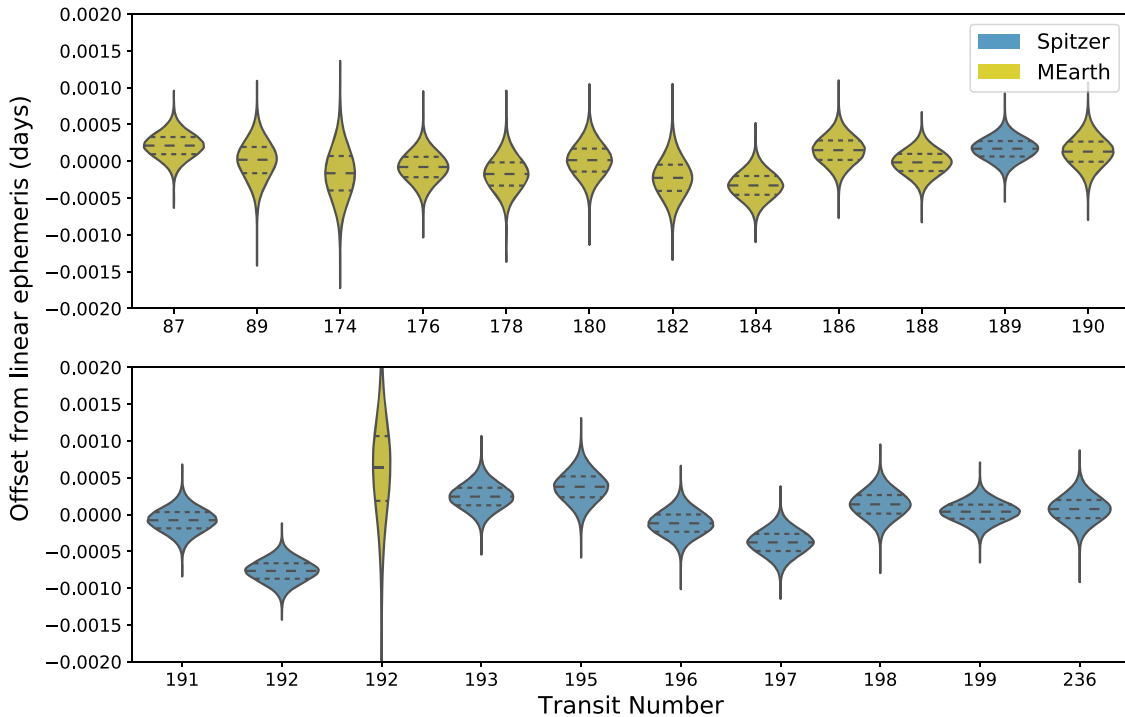
Figure 5. Violin plot showing distribution of simulated mid-transit times (in days) from the MCMC analysis. Transits are shown individually (denoted by the transit number, counting up from the transit ephemeris given in Mann et al. 2016), and the width of the distribution indicating the probability density of the mid-transit time as that vertical location. The dashed line marks the 50th percentile and the dotted lines show the 16th and 84th percentiles. The spread of the distribution for MEarth transit 192 can be attributed to moderate data quality.
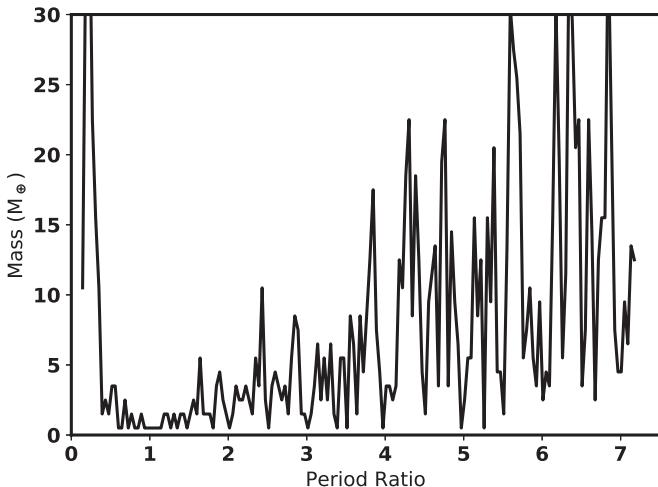
Figure 6. Mass of a perturbing object vs. orbital period ratio required to create a 2 minute TTV signal in K2-25b. We marginalize over eccentricity, orbital inclination, longitudinal node, argument of periapsis, and mean anomaly of the orbit using the `TTVFaster` code. We find that companions out to the 2:1 mean-motion resonance are inconsistent with the observed transit times from MEarth, *Spitzer*, and K2. Super-Earth-mass companions and smaller can be consistent with our transit timing data out to ~7:2 period ratios. Beyond the 7:2 resonance, only companions in integer period ratios with K2-25b can be ruled out.

in its lifetime. If, however, this timescale is much less than the age of the system, then it could be that the eccentricity is being actively excited.

6.1. Circularization Timescale

We use the mass estimation determined in the previous section to calculate the circularization timescale of this system,

the approximate amount of time it would take tidal forces to damp K2-25b's eccentricity. We use the equation derived in Goldreich et al. (1966) as presented in Equation (2) of Jackson et al. (2009), with a negative sign on the second term due to the star's rapid spin:

$$\tau_{\rm circ} = a^{13/2} \left(\frac{63}{4} \sqrt{GM_*^3} \frac{R_P^5}{Q_P' M_P} - \frac{225}{16} \sqrt{G/M_*} \frac{R_*^5 M_P}{Q_*'} \right)^{-1},$$

(1)

where M_P is the planet mass, R_P is the planet radius, M_* is the stellar mass, and a is the semimajor axis. Values of Q_P' and Q_*', the modified tidal quality factors of the planet and the star ($Q' = 2Q/3k$), are not well constrained. Q_*' values inferred from the circularization of hot Jupiters and stellar binaries vary (see discussion and references in Mathis 2018). For K2-25, the tides raised by the star on the planet dominate and the term involving Q_*' is negligible.

We estimate a circularization timescale of 410 Myr using $Q_P' = 5 \times 10^4$ and the mass as determined in the previous section. Based on the 68% confidence interval of the masses, the 68% confidence interval of the circularization timescale is 180 Myr to 1 Gyr. Our selected Q_P' is based on Neptune's Q_N/k value of $2.2 \times 10^4 < Q_N < 9 \times 10^4$ from Zhang & Hamilton (2008). Varying Q_P' by an order of magnitude adjusts the calculated timescale by an order of magnitude as well. If K2-25b is in fact a higher density world, we would expect its mass to be greater and its Q_P' to be lower. For $M_P = 30 M_\oplus$ and $Q_P' = 100$, the circularization timescale is only 4 Myr.

We note that the K2-25 system is unlike many other planetary systems in that the star is rotating faster ($P_* = 1.88$ days) than the planet orbits ($P_P = 3.48$ days), driving the negative sign on the second term in Equation (1). An extended

period of rapid rotation like K2-25's is common to all mid-to-late M dwarfs, though most known M-dwarf planet hosts are presently slowly rotating (Newton et al. 2016). Q_* is a parameterization of the tidal response of the star, and is influenced by the frequencies at which the star spins and the planet orbits (Ogilvie & Lin 2007). In some extreme cases, the planetary eccentricity can be excited rather than damped (Dobbs-Dixon et al. 2004). Using the equations in Dobbs-Dixon et al. (2004), we find that K2-25 is not in this regime; a several Jupiter mass planet would be required.

6.2. Migration Mechanisms

The eccentric orbit of K2-25b suggests a dynamical past. While some authors argue that planets in this radius range can be formed in situ, these simulations do not generally yield eccentricities as high as that observed for K2-25b (Ogihara et al. 2015; Lee & Chiang 2016). On the other hand, Moriarty & Ballard (2016) find that disks with shallow surface density profiles produce systems where only one planet will typically transit, where planets have large eccentricities, obliquities, and spacings. In their simulations, the planets in these systems are separated by 20–60 Hill radii. K2-25b could be an example of such a system; in this case we might expect a second planet with $P \lesssim 15$ days that likely does not transit. Our TTV analysis rules out many planets within this period range, but has a limited mass sensitivity near 15 days.

Alternatively, K2-25b could have arrived at its present orbit via a high-eccentricity migration mechanism, which has been proposed as a mechanism of inward migration for hot Jupiters (see Dawson & Johnson 2018, for an overview). This process involves two steps: the orbital momentum of the planet is reduced by a perturber, decreasing periastron distance and exciting eccentricity; then its orbital energy is reduced due to tidal dissipation, drawing the planet inward. After this close-in eccentric system is created, its orbit is eventually circularized.

6.3. Future Outlook

Further constraints on the presence of a companion require new data. Long-term radial velocity or astrometric monitoring would place additional constraints on the existence of a companion. Mann et al. (2016) found no periodic signals at periods <20 days in the *K2* data, and no additional transit-like signals were seen in a by-eye inspection. Measurements of the Rossiter-McLaughlin effect would indicate whether the planetary orbit is aligned with the host star, or if it is misaligned as in the case of Gl 436b (Bourrier et al. 2018). Significant spin–orbit misalignment and retrograde motion could result from certain high-eccentricity migration scenarios (e.g., Naoz et al. 2012; Li et al. 2014; Storch et al. 2017).

7. Summary

K2-25b is an eccentric hot Neptune in the Hyades cluster. We obtained multiyear photometric monitoring and 12 transit lightcurves using the MEarth observatories. Combing our data with those from *Spitzer*, our data set consists of 22 nonconsecutive transits. The MEarth data are available in a online table. We fit for r_P/R_* and the transit times T using the `batman` tool and `emcee` MCMC package. Our transit time measurements can be found in Table 6.

We find that the amplitude of photometric variability was high, at around 2% peak-to-peak, during the *K2* campaign and the ground-based observing in 2015–2016. From 2016 to 2018, when most of our transit observations occurred, the variability is significantly diminished; this highlights the importance of long-term photometric monitoring. Despite the number of transits and the presumed overall spottiness of the star, we do not definitively identify spot crossings. There is tentative evidence of a spot crossing in one transit in the *Spitzer* data, and two transits from MEarth show systematic deviations from the fiducial transit model.

The uncertainty in Q_P and the planetary mass, and thus in the circularization timescale τ_{circ}, makes it challenging to establish whether K2-25b's eccentricity requires ongoing excitation. However, for Neptunian values of Q_P, the age of the planetary system (650 Myr) is similar to τ_{circ} (410 Myr; 68% confidence interval: 180 Myr to 1 Gyr).

Our measured transit times show no evidence for TTVs. On this basis, we can exclude roughly Earth-mass companions out to the 2:1 period ratio, and super Earths with masses $>5\,M_\oplus$ out to the 7:2 period ratio. Save for in strong resonances, TTVs do not provide strong constraints on companions at longer periods.

ORCID iDs

Isabel J. Kain ⓘ https://orcid.org/0000-0001-9894-5229
Elisabeth R. Newton ⓘ https://orcid.org/0000-0003-4150-841X
Jason A. Dittmann ⓘ https://orcid.org/0000-0001-7730-2240
Andrew W. Mann ⓘ https://orcid.org/0000-0003-3654-1602
Pa Chia Thao ⓘ https://orcid.org/0000-0001-5729-6576
David Charbonneau ⓘ https://orcid.org/0000-0002-9003-484X
Jennifer G. Winters ⓘ https://orcid.org/0000-0001-6031-9513

References

Agol, E., Steffen, J., Sari, R., & Clarkson, W. 2004, MNRAS, 359, 567
Aigrain, S., Parviainen, H., & Pope, B. 2016, MNRAS, 459, 2408
Ballard, S., Fabrycky, D., Fressin, F., et al. 2011, ApJ, 743, 200
Barnes, J. 2007, PASP, 119, 986
Basri, G. 2018, ApJ, 865, 142
Batygin, K., Laughlin, G., Meschiari, S., et al. 2009, ApJ, 699, 23
Bourrier, V., Lovis, C., Beust, H., et al. 2018, Natur, 553, 477
Brandt, T. D., & Huang, C. X. 2015, ApJ, 807, 24
Butler, R. P., Vogt, S. S., Marcy, G. W., et al. 2004, ApJ, 617, 580
Collaboration, A., Price-Whelan, A. M., Sipőcz, B. M., et al. 2018, AJ, 156, 19
David, T. J., Hillenbrand, L. A., Petigura, E. A., et al. 2016, Natur, 7609, 658
Dawson, R. I., & Johnson, J. A. 2012, ApJ, 756, 122
Dawson, R. I., & Johnson, J. A. 2018, ARA&A, 56, 175
Deck, K. M., & Agol, E. 2016, ApJ, 821, 96
Deck, K. M., Agol, E., Holman, M. J., & Nesvorný, D. 2014, ApJ, 787, 132
DeGennaro, S., von Hippel, T., Jefferys, W. H., et al. 2009, ApJ, 696, 12
Deming, D., Knutson, H., Kammer, J., et al. 2015, ApJ, 805, 132
Dittmann, J. A., Close, L. M., Green, E. M., & Fenwick, M. 2009, ApJ, 701, 756
Dittmann, J. A., Irwin, J. M., Charbonneau, D., Berta-Thompson, Z. K., & Newton, E. R. 2017, AJ, 154, 142
Dittmann, J. A., Irwin, J. M., Charbonneau, D., & Newton, E. R. 2016, ApJ, 818, 153
Dobbs-Dixon, I., Lin, D. N. C., & Mardling, R. A. 2004, ApJ, 610, 464
Dong, S., Xie, J.-W., Zhou, J.-L., Zheng, Z., & Luo, A. 2018, PNAS, 115, 266
Douglas, S. T., Agüeros, M. A., Covey, K. R., et al. 2014, ApJ, 795, 161
Fazio, G. G., Hora, J. L., Allen, L. E., et al. 2004, ApJS, 154, 10
Ford, E., Quinn, S., & Veras, D. 2008, ApJ, 678, 1407
Ford, E. B. 2014, PNAS, 111, 12616
Foreman-Mackey, D., Hogg, D. W., Lang, D., & Goodman, J. 2013, PASP, 125, 306
Gaia Collaboration, Babusiaux, C., van Leeuwen, F., et al. 2018, A&A, 616, A10
Goldreich, P., Soter, S., & Cameron, A. G. W. 1966, Icar, 5, 375
Goodman, J., & Weare, J. 2010, CAMCS, 5, 65
Gossage, S., Conroy, C., Dotter, A., et al. 2018, ApJ, 863, 67
Holman, M. J., & Murray, N. W. 2005, Sci, 307, 1288
Hunter, J. D. 2007, CSE, 9, 90
Ingalls, J. G., Krick, J. E., & Carey, S. J. 2012, Proc. SPIE, 8442, 84421Y
Irwin, J., Irwin, M., Aigrain, S., et al. 2007, MNRAS, 375, 1449
Irwin, J. M., Berta-Thompson, Z. K., Charbonneau, D., et al. 2015, in Conf. Proc. 18th Cambridge Workshop on Cool Stars, Stellar Systems, and the Sun, ed. G. van Belle & H. C. Harris (New York: Springer), 767
Jackson, B., Barnes, R., & Greenberg, R. 2009, ApJ, 698, 1357
Kanodia, S., Wolfgang, A., Stefansson, G. K., Ning, B., & Mahadevan, S. 2019, ApJ, 882, 38
Kipping, D. M. 2013, MNRAS, 435, 2152
Kreidberg, L. 2015, PASP, 127, 1161
Lee, E. J., & Chiang, E. 2016, ApJ, 817, 90
Lewis, N. K., Knutson, H. A., Showman, A. P., et al. 2013, ApJ, 766, 95
Li, G., Naoz, S., Holman, M., & Loeb, A. 2014, ApJ, 791, 86
Mandel, K., & Agol, E. 2002, ApJ, 580, L171
Mann, A. W., Gaidos, E., Mace, G. N., et al. 2016, ApJ, 818, 46
Martín, E. L., Lodieu, N., Pavlenko, Y., & Béjar, V. J. S. 2018, ApJ, 856, 40
Mathis, S. 2018, in Handbook of Exoplanets, ed. H. Deeg & J. Belmonte (Cham: Springer), 24
Melo, C., Santos, N. C., Gieren, W., et al. 2007, A&A, 467, 721
Moriarty, J., & Ballard, S. 2016, ApJ, 832, 34
Murray-Clay, R. A., Chiang, E. I., & Murray, N. 2009, ApJ, 693, 23
Naoz, S., Farr, W. M., & Rasio, F. A. 2012, ApJ, 754, L36
Newton, E. R., Irwin, J., Charbonneau, D., et al. 2016, ApJ, 821, 93
Ning, B., Wolfgang, A., & Ghosh, S. 2018, ApJ, 869, 5
Ogihara, M., Morbidelli, A., & Guillot, T. 2015, A&A, 578, A36
Ogilvie, G. I., & Lin, D. N. C. 2007, ApJ, 661, 1180
Perryman, M. A. C., Brown, A. G. A., Lebreton, Y., et al. 1998, A&A, 331, 81
Rackham, B. V., Apai, D., & Giampapa, M. S. 2018, ApJ, 853, 122
Sanchis-Ojeda, R., & Winn, J. N. 2011, ApJ, 743, 61
Santos, N. C., Santerne, A., Faria, J. P., et al. 2016, A&A, 592, A13
Storch, N. I., Lai, D., & Anderson, K. R. 2017, MNRAS, 465, 3927
Thao, P. C., Mann, A., & Newton, E. 2020, AJ, 159, 32
Waskom, M., Botvinnik, O., O'Kane, D., et al. 2018, mwaskom/seaborn: v0.9.0 (July 2018), Zenodo, doi:10.5281/ZENODO.1313201
Wolfgang, A., Rogers, L. A., & Ford, E. B. 2016, ApJ, 825, 19
Zhang, K., & Hamilton, D. P. 2008, Icar, 193, 267